

Heat transfer coefficient distribution on the pole face of a hydrogenerator scale model

F. Torriano ^{a,*}, N. Lancial ^{b,c,d}, M. Lévesque ^a, G. Rolland ^d, C. Hudon ^a, F. Beaubert ^{b,c}, J.-F. Morissette ^a, S. Harmand ^{b,c}

^a Institut de recherche d'Hydro-Québec, Varennes, Canada

^b Université Lille Nord-de-France, Lille, France

^c UVHC TEMPO/DF2T, Valenciennes, France

^d Électricité de France R&D, Clamart, France



HIGHLIGHTS

- Temperature measurements and 3D simulations of the pole of a hydrogenerator scale model were done.
- Lower heat transfer coefficient values are found closer to the trailing edge of the pole.
- The highest heat transfer coefficient values are found in an intermediate region of the pole.
- Heat transfer coefficients along the pole face at 300 rpm average about four times those at 50 rpm.

ARTICLE INFO

Article history:

Received 31 December 2013

Accepted 19 April 2014

Available online 10 May 2014

Keywords:

Hydrogenerator

Heat transfer coefficient

Salient pole machine

FEM

CFD

ABSTRACT

This paper focuses on the effect of rotation on heat transfer mechanisms in rotating machines with the purpose to improve the understanding of thermal phenomena and cooling of hydrogenerators. Using a simplified scale model equipped with a heated pole, it was possible to measure the temperature distribution on the pole surface and to deduce, through numerical simulations, the heat transfer coefficients. The results show an asymmetric profile in the tangential direction since lower h values are found closer to the trailing edge due to the presence of a flow recirculation zone. Furthermore, the heat transfer profiles indicate that, although fans improve cooling at the top and bottom ends of the pole, the highest h values are found in an intermediate region. This is due to the flow from the fans that enters the interpole space and only after penetrating a certain distance in the axial direction it exits through the air gap and goes around the pole face. The study also shows that the heat transfer coefficients along the pole face at 300 rpm average about four times those at 50 rpm.

© 2014 Elsevier Ltd. All rights reserved.

1. Introduction

Salient pole synchronous machines are essential to convert the mechanical energy of water turbines into electrical energy. One of the most common causes of reduced hydrogenerators service life is deterioration of insulation material due to overheating. It is thus critical to monitor temperatures during operation to ensure that the hot-spot value does not exceed the critical limit. Moreover, since overheating is often caused by poor circulation of the cooling fluid, it is necessary to understand the flow dynamics and heat transfer mechanisms in the various generator components (i.e.,

end-winding, pole face, etc.). A hybrid approach, based on experimental measurements and numerical simulations, is needed to improve the understanding of thermofluid phenomena as the numerical methods have not yet achieved sufficient maturity to be used alone. In fact, the mesh size required to discretize the computational domain may reach 100 million elements and modeling phenomena such as turbulence remains quite complex. On the other hand, experimental measurements require a considerable instrumentation effort and access to prototypes is often limited. A laboratory scale model thus appears to be the best solution to acquire data in order to validate numerical models. This approach was chosen by IREQ (Institut de recherche d'Hydro-Québec), EDF (Électricité de France) and TEMPO/DF2T (Université Lille Nord-de-France) which developed a common strategy to share knowledge in the field of hydrogenerators thermofluid analysis.

* Corresponding author.

E-mail address: torriano.federico@ireq.ca (F. Torriano).

Nomenclature		
Bi	Biot number he/k	
c_p	specific heat at constant pressure ($J \text{ kg}^{-1} \text{ K}^{-1}$)	
d	air gap dimension (m)	
e	thickness (m)	
h	heat transfer coefficient ($\text{W m}^{-2} \text{ K}^{-1}$)	
k	thermal conductivity ($\text{W m}^{-1} \text{ K}^{-1}$)	
q	heat power (W)	
q''	heat flux (W m^{-2})	
q''_{rad}	radiation heat flux (W m^{-2})	
q'''	volumetric heat source (W m^{-3})	
r	radius (m)	
$R''_{t,c}$	thermal contact resistance ($\text{m}^2 \text{ K W}^{-1}$)	
Re	Reynolds number = $\omega r_{\text{rotor}} d / \nu$	
T_s	surface temperature ($^{\circ}\text{C}$)	
T_{∞}	adjacent air temperature ($^{\circ}\text{C}$)	
<i>Greek symbols</i>		
δ_E	energy conservation criterion at interface (%)	
ΔT	temperature difference ($^{\circ}\text{C}$)	
ϵ	surface emissivity	
θ	angular coordinate (deg)	
ν	kinematic viscosity ($\text{m}^2 \text{ s}^{-1}$)	
ρ	density (kg m^{-3})	
σ	Stefan–Boltzmann constant = $5.670 \times 10^{-8} (\text{W m}^{-2} \text{ K}^{-4})$	
ω	angular velocity (rad s^{-1})	

A number of papers have been published about thermofluid analysis of electrical machines and as discussed by Boglietti et al. [1], lumped-parameter thermal network (LPTN), finite element method (FEM) and computational fluid dynamics (CFD) approaches are now used by both manufacturers and utilities. LPTN is the oldest numerical approach but still the most commonly used to obtain a fast analysis with a relatively low computational effort, as shown by Dajaku et al. [3]. Traxler et al. [17] have also developed advanced computational methods for the calculation of temperatures with thermal flow networks coupled to cooling airflow networks in order to identify hot-spots quite accurately. Fasquelle et al. [6] have proposed a multi-physical model to take into account electromagnetic, mechanical and thermofluid phenomena in an induction motor. The thermofluid modeling is based on an equivalent thermal circuit and flow dynamics inside the machine is obtained by CFD computation.

Finite element method can also be used to calculate more accurately heat conduction in complex geometric shapes and has become a standard tool, especially for electromagnetic analysis. For example, Fan et al. [5] studied local rotor temperature rises using 3D FEM computations from a 2D electromagnetic field model of a bulb-type hydrogenerator. Furthermore, Weili et al. [20] calculated the 3D electromagnetic field using 3D FEM computations and then obtained the temperature distribution in the turbogenerator through a conjugated heat transfer simulation.

Computational fluid dynamics is the most recent technique and its application to hydrogenerators was made possible by the computing power available today. Papers have been published on CFD simulation of electrical machines such as Lang et al. [11] and Ujiie et al. [18] who simulated the cooling airflow and calculated convective heat transfer in different components. Depraz et al. [4] compared CFD and network models and found good agreement. Pickering et al. [13] also conducted a validation study comparing measured and predicted local heat transfer coefficients (h). CFD well predicted the overall trend of the heat transfer coefficient on the pole surface but computed values were up to 30% lower than the measured ones. According to Shanel et al. [16], more accurate solutions can be obtained using a conjugate heat transfer (CHT) computation where flow and thermal simulations are coupled. Vogt et al. [19] have performed a CFD simulation of the cooling circuit of a large hydrogenerator and the results have been used as input for a detailed CHT simulation of the stator core. However, this type of simulation is very computationally expensive and presently not feasible in a prototype design process, as discussed in Kastner et al. [10].

Some authors have performed experiments to determine heat transfer coefficients on active components of a generator and

Carew [2] has obtained correlations for heat transfer coefficient on the leading and trailing faces of a salient pole. The author also compared measured values with semi-empirical equations from earlier studies and found acceptable agreement. Robinson et al. [14] have also made heat transfer measurements on a salient pole generator and have developed empirical formulae for the heat transfer coefficient on the pole sides and pole face. The authors found that heat transfer on the pole sides depends on the ratio of axial to tangential velocity whereas on the pole face the tangential velocity is the main factor affecting heat transfer. In a similar study by Murata et al. [12], temperatures on a four-pole synchronous generator were measured and equations derived for the heat transfer coefficient on the pole surface. In all these studies, the local heat transfer coefficient was found to vary significantly across the pole surface and to have a strong dependence upon the rotational speed. Recently, Fénot et al. [7] have measured heat transfer on the surface of a four-slots rotating cylinder placed in an annular channel. The heat transfer correlations that were obtained showed an axial speed as well as radial speed dependency. Moreover, heat transfer was found to be higher on the leading edge than on the trailing edge of the rotor pole. Lastly, Huang et al. [8] have shown the validity of using an inverse algorithm to compute the time-dependent heat flux on the rotor and stator surfaces of a high speed electric motor.

This paper continues to invest the effect of rotation on convection heat transfer at the surface of a hydrogenerator pole in order to improve understanding of flow and thermal transfer phenomena on electrical machines. With the IREQ scale model of a hydrogenerator, temperature profiles on the rotor pole face have been measured and the heat transfer coefficient distribution was obtained from numerical simulation using both commercial code Ansys-CFX and in-house EDF code SYRTHE 4.0. The paper is divided into four main sections. The scale model design is first presented and then the measuring apparatus. Next, the methodology to obtain, through numerical simulations, the heat transfer coefficient from temperature measurements is described. Lastly, experimental and numerical results are analyzed.

2. Experimental setup

Due to limited access to an actual generator and challenges in performing thermal and flow measurements on one, available data is insufficient to validate numerical models and to help understand complex phenomena such as heat transfer in rotating parts of the machine. For these reasons, a scale model was designed and built at IREQ based on generators in service at Hydro-Québec. The scale model is simplified in that it lacks the active electromagnetic

elements of the prototype, but it does include all main ventilation components.

As illustrated in Fig. 1, the scale model is placed inside an enclosure in order to have a closed-loop ventilation circuit. The rotor spider acts as a pump that drives the flow through the rotor rim and fan blades, then through the air gap, stator and stator frame. Air exits the stator frame through four openings, where deflector plates redirect the flow in the radial direction. Finally, the air in the enclosure returns to the rotor from the top or bottom openings. The main simplifications in the scale model include the omission of radiators and the use of a slotted cylindrical transparent plate as the stator in order to view rotor components, more easily visualize the flow and enable PIV (particle image velocimetry) measurements. For these reasons, many other components are also made of transparent material. Simplifications were primarily made to facilitate measurements as well as to reduce geometric complexity in order to ease the meshing process of the numerical study. For example, the winding is not present on the pole (i.e., the pole surface is smooth) but in the future it is planned to apply various patterns of surface roughness on the pole sides to mimic the presence of coils and to determine their effect on the flow and heat transfer.

Furthermore, the scale model was designed so it could be easily modified and parts replaced in order to test different ventilation schemes and to determine the impact of specific components on windage losses and flow distribution. Possible changes include replacing the fan blade, adjusting the area of the top and bottom openings and reducing the number and size of rim and stator ducts.

Although the overall dimensions are scaled down (1:4 in the radial direction and 1:2 in the axial direction), such key components as the air gap, rim ducts and stator ducts are the same size as those in the actual generator in order to maintain dynamic similarity with the prototype and facilitate the installation of flow sensors (see Table 1). A 75 HP electrical motor drives the rotor clockwise up to a maximum speed of 500 rpm to maintain prototype similitude of the local Reynolds number in the air gap ($Re \approx 50\,000$). Since the operating air temperature in the enclosure may exceed 60 °C due to heat generated by the windage losses, external fans are placed around the enclosure to provide sufficient cooling and to maintain temperatures within the target range.

The scale model is also used to analyze heat transfer phenomena on the surface of a rotor pole, so one pole is equipped with independent heating elements in order to generate a heat flux at its surface. The heating pattern can be varied and the surface temperature is measured with thermistors and a high-frequency

Table 1
Scale model characteristics.

Rotor diameter	2.270 m
Rotor height	1.040 m
Number of rotor ducts	36 × 23
Dimension of rotor ducts	23 × 12.7 mm
Number of poles	36
Stator inner diameter	2.296 m
Stator thickness	4.76 mm
Stator height	0.73 m
Number of stator ducts	72 × 29
Dimension of stator ducts	43 × 6 mm
Number of radiator openings	4
Enclosure dimensions	3.2 × 3.2 × 1.8 m

pyrometer probe placed in the stator ducts. This data yields the heat transfer coefficient distribution on the pole surface.

As shown in Fig. 2b), the rotor poles are made of a thin 304 stainless steel shell ($e = 0.912$ mm) that is riveted onto seven aluminum rim supports to ensure mechanical strength (see Fig. 2a)). The poles are thus empty inside and this has allowed the installation of 18 heating pads inside one of them to generate a heat flux at its surface (see Fig. 2c)). The heating pads, positioned to maximize the heated surface of the pole (see Fig. 3a)), are of four power categories and two sizes, smaller on the sides (54 W or 83 W max.) and larger on the pole face (148 W or 225 W max.). The power of each heating element can be adjusted to obtain the desired heating pattern with current supplied to the pads via a slip ring attached to the rotor shaft.

Each heating element is composed of a serpentine copper wire (resistance) inside a silicone matrix 1.27 mm thick (orange layer in the web version in Fig. 3b)). Insulating foam 6.35 mm thick (brown layer in the web version in Fig. 3b)) is placed on the back of the pad to force the heat flux towards the front face of the pole shell. The heating elements are fixed on the stainless steel shell with silicone based glue (RTV 157). A layer of about 1 mm is applied to ensure sufficient adhesion (grey layer in Fig. 3b)). Thermally conductive glue would have been preferable but due to the extremely high centrifugal forces (350 g at 500 rpm) and high temperatures (150 °C) to which the pads are subjected, RTV silicone was the only suitable glue. The silicone glue thickness of 1 mm was chosen based on a series of tests (not presented here) aimed at minimizing the amount of silicone (for heat transfer purposes), while providing sufficient adhesion to the metallic shell. Moreover, measurements were made with an infrared camera to verify the temperature uniformity as well as the insulation capability of the foam on the back of the pads.

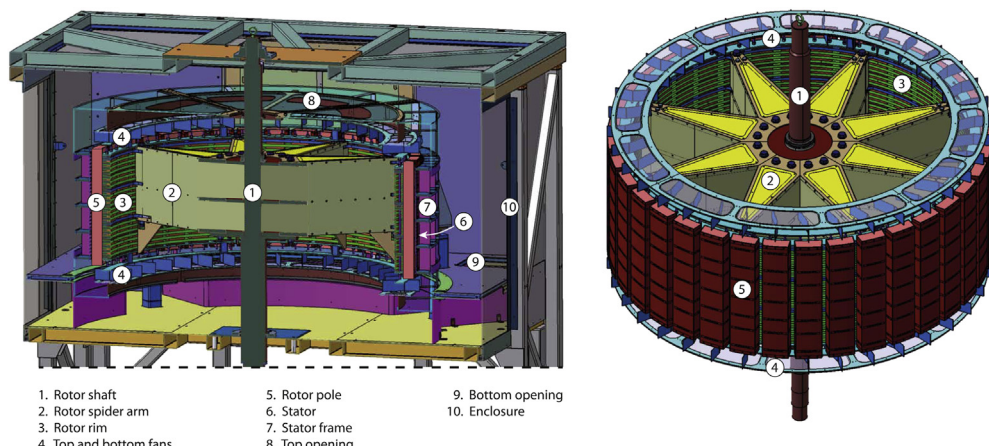


Fig. 1. Generator scale model.

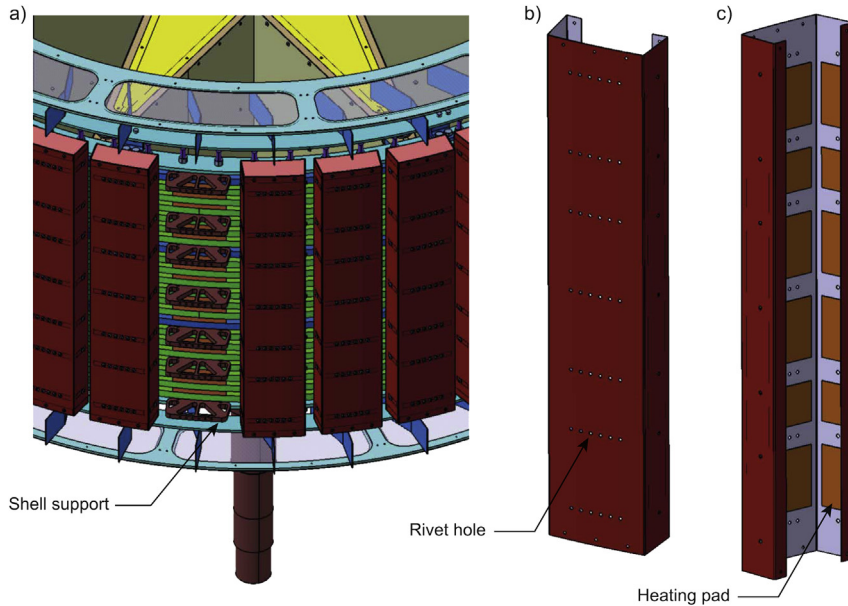


Fig. 2. Pole shell with heating pads.

Since the heated pole is about 1 kg heavier and at a much higher temperature than the other poles, thermo-mechanical simulations were carried out with Ansys software to ensure that scale model integrity was maintained and that mechanical (centrifugal) and

thermal (expansion) stresses did not exceed the elastic limit of steel. From the results, it was decided to change the type of steel for the heated pole (4130 instead of 304) and also to increase the shell thickness (1.27 mm instead of 0.912 mm). Finally, “black oxyde”

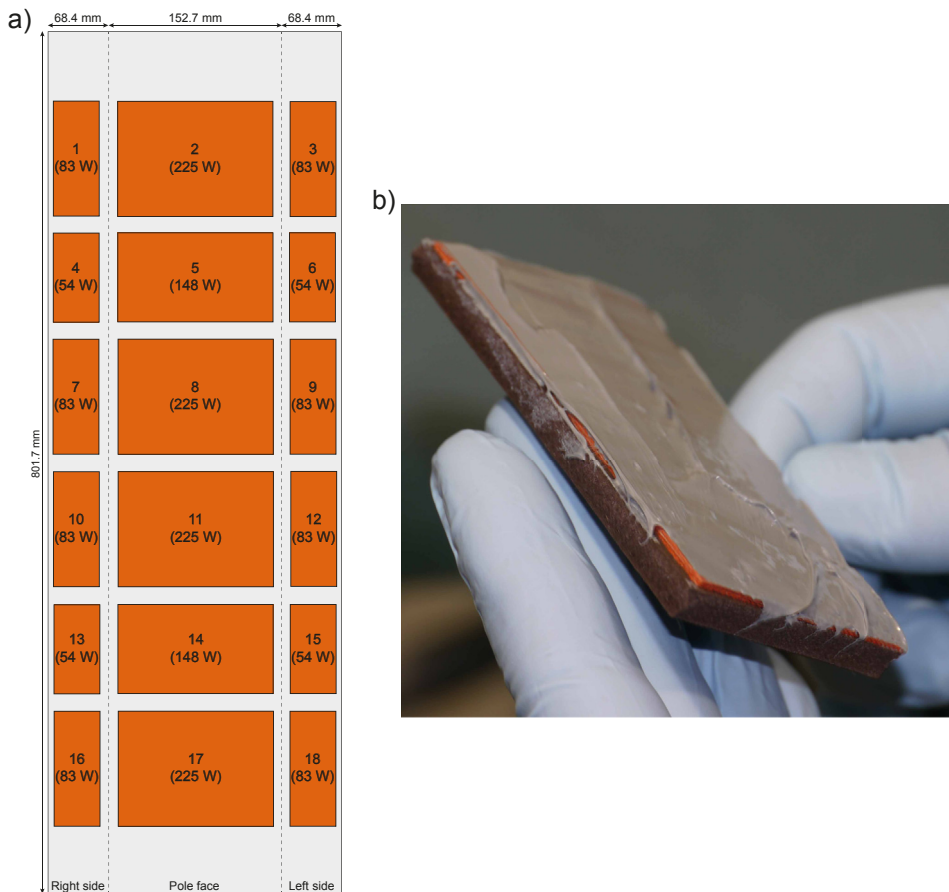


Fig. 3. Position and power of the heating pads (a); heating pad assembly (b).

treatment was applied on the outer shell surface to have better surface emissivity for infrared measurements.

3. Instrumentation

As mentioned in the previous section, the main goal of installing heating elements on a pole is to determine the heat transfer coefficient along the pole surface. To do so adequately, it is important to have a sufficient numbers of temperature sensors. Fig. 4(a) shows the position of the 84 thermistors and 2 surface RTDs (resistance thermal detectors) installed. The RTDs allow the pole temperature to be monitored in real time in order to ensure that the maximum allowable temperature (150°C) is never reached during the tests. A Datatel communication module and Graphtec acquisition module are used for data transmission. The thermistor temperatures are recorded every 15 s on a Datalogger module mounted on the rotor shaft (see Fig. 4(c)) and downloaded to a PC at the end of a test run. The thermistors are secured to the inner shell surface by means of thermally conductive ceramic glue.

Although the objective is to measure the temperature distribution on the outer surface of the pole, the sensors could not be

installed there since they and their wiring would have greatly perturbed the cooling flow, thus biasing the temperature measurement itself. Consequently, by knowing the heat flux q'' , it is possible to obtain from the Fourier law ($q'' = k \Delta T/e$) the temperature on the outer surface from inner surface measurements. Moreover, due to the small shell thickness and quite good thermal conductivity of stainless steel the temperature gradient between the inner and outer surfaces of the shell is expected to be small ($Bi \ll 1$).

In addition to thermistors, the pole face temperature is also measured with a VibroSystM ThermaWatch® Rotor infrared sensor for higher spatial resolution. As illustrated in Fig. 4(b), the probe consists of a long rod which is inserted into the stator ducts up to a distance of 13 mm from the pole face in order to place the probe tip very close to the surface to be monitored. The sensor can measure temperatures from 0°C to 200°C and has a high sampling rate (10 kHz). That rates provides fine spatial resolution in the circumferential direction (i.e., the pole width) even at 500 rpm. Spatial resolution in the axial direction is limited by the number of stator ducts (26) through which the ThermaWatch® Rotor can be inserted. Since pyrometer measurements are affected by the surface

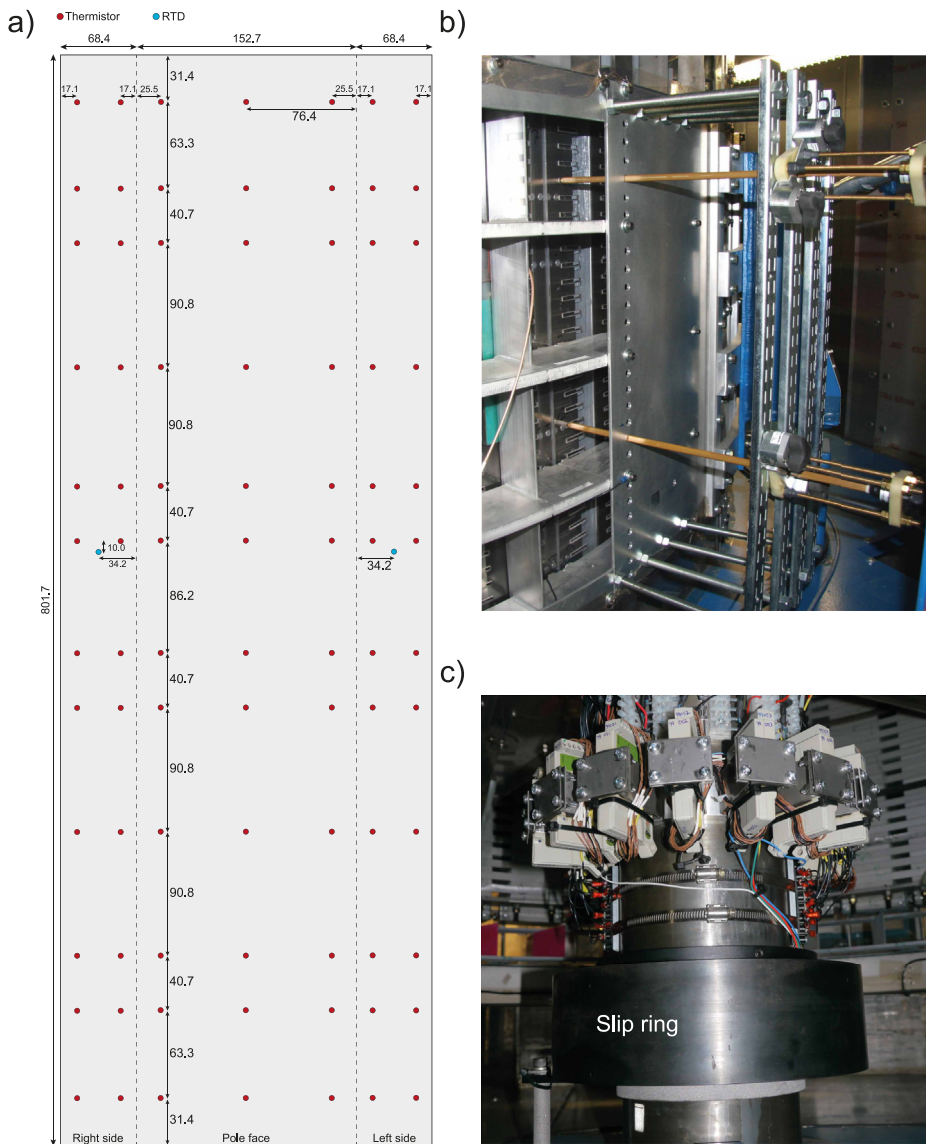


Fig. 4. Position (in mm) of temperature sensors on the pole shell (a), ThermaWatch® Rotor (b) and Datalogger system (c).

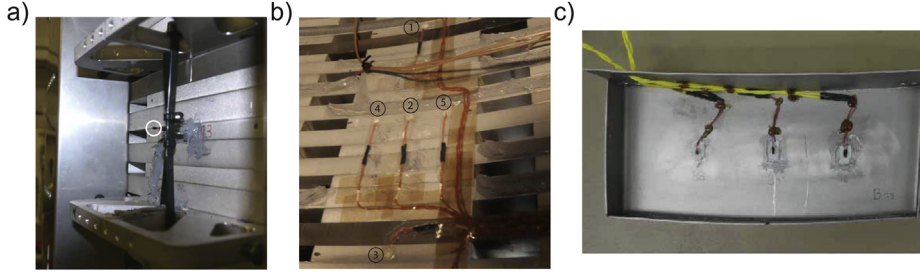


Fig. 5. Thermistors in the air inside the shell (a), on pole supports (b) and on the pole cover (c).

emissivity, the sensor was calibrated prior to its installation in the scale model. Unfortunately, the temperature distribution on the sides of the pole cannot be measured with this technique since the surface must be perpendicular to the probe axis.

Though heat generated by the pads is mainly dissipated by forced convection through the external surface of the pole, a percentage of the heat flux is directed toward other components such as the top and bottom shell covers, the air inside the shell and the aluminum shell supports. In order to determine the fraction of the total heat flux that is lost through those components, three thermistors were placed on the top and bottom covers (see Fig. 5(c)) and two on the outer and inner radius of the central shell support. Each support is also equipped with a thermistor on the centroid of the inner surface in order to measure the temperature in the section that is pressed between the rim plates (1, 2 and 3 in Fig. 5(b)). The central support has two additional thermistors at 1/4 and 3/4 of the width to verify the tangential temperature uniformity (4 and 5 in Fig. 5(b)). Moreover, a sensor was installed between two supports to measure the air temperature inside the shell (see Fig. 5(a)). Lastly, two thermistors were placed in the interpolar space to either side of the heated pole and a third 5 mm from the pole face to measure the air temperatures in the interpole and the air gap respectively.

4. Numerical model

In this section, the numerical approach used to obtain the heat transfer coefficient distribution on the pole surface from the temperature measurements is described in detail. The heat transfer

equation is defined by $q'' = h \Delta T$ where q'' is the heat flux at the pole surface and ΔT is the temperature difference between the external shell surface temperature (T_s) and the adjacent air temperature (T_∞). The pole surface temperature can be obtained with the thermistors and the ThermaWatch® Rotor measurements but the heat flux distribution is not known a priori since the only available data is the power dissipated by each heating element. For this reason, it is necessary to build a numerical model of the heated pole that computes the heat flux distribution and consequently allows the heat transfer coefficient to be evaluated over the entire pole surface.

As shown in Fig. 6, a CAD model was built including the covers, supports, silicone glue and three layers composing the heating pads. For the Ansys-CFX calculation, a structured hexahedral mesh was generated with Ansys-Icem except for the supports which were meshed with the unstructured hexahedral mesher of Ansys-Workbench. The overall mesh size is 5 111 000 cells of which 1 518 000 elements discretize the shell itself. In general, the mesh refinement gives an average cell size of 1 mm in the x and y-direction and 2 mm in the axial direction, except for the shell thickness ($e = 1.27$ mm) where ten elements are used.

Since the covers, supports, silicone layer and heating pads are meshed independently, “solid–solid” general grid interfaces (GGI) are used to connect the various components and an energy conservation criterion ($\delta_E < 1\%$) is specified at each interface.

A different meshing approach had to be used for the SYRTHES 4.0 computations since this finite element solver can only accept tetrahedral meshes in 3D according to Rupp et al. [15]. The grid was generated with SALOME 6.0 and has an overall size of 6 197 000

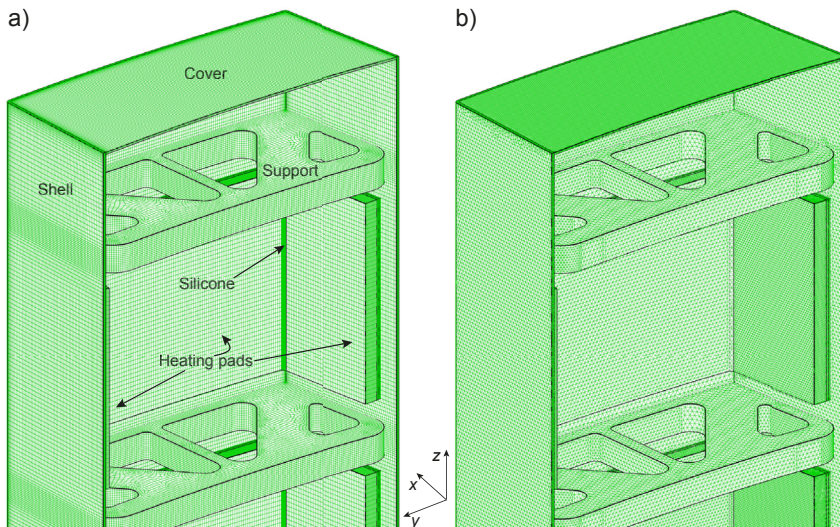


Fig. 6. Computational mesh: Ansys (a) and SALOME 6.0 (b).

Table 2

Heat flux as a function of thermal contact resistance at support–shell interface.

$R''_{t,c}$ ($\text{m}^2 \text{K W}^{-1}$)	q''_{tot} (W m^{-2})	$q''_{\text{pole face}}$ (W m^{-2})	$q''_{\text{pole sides}}$ (W m^{-2})	$q''_{\text{rad tot}}$ (W m^{-2})	$q''_{\text{interf. supports}}$ (W m^{-2})
0.05	589.4	293.1	211.5	43.1	9.7
0.001	589.4	241.3	172.6	34.2	117.4
0.0005	589.4	234.4	166.0	33.0	133.3
0.0001	589.4	227.0	157.9	31.5	151.8
0.00005	589.4	225.5	156.2	31.2	155.5

elements. Element dimensions are about 2 mm in all three directions but ten elements are set in the shell thickness. Since the entire domain is meshed as a single block, there are no interfaces to specify between the pole components. It should be mentioned that a mesh-independence study was performed for both Ansys-CFX and SYRTHES 4.0 in order to ensure that the grid resolution was appropriate.

For both solvers, a volumetric heat source (q''') is specified in each heating pad. Boundary conditions are also required on all the surfaces inside the shell, but the temperature is not directly measured in these regions since that would have required too many sensors. Since the surfaces inside the shell are in contact with stagnant air, empirical formulae for natural convection on vertical or horizontal plates were obtained from Ref. [9] to determine the respective heat transfer coefficients (values vary between 2 and 9 $\text{W m}^{-2} \text{K}^{-1}$). The air temperature inside the shell is measured by a thermistor. On the inner surface of the supports, either a heat transfer coefficient or a temperature is specified.

For the external pole surface, the temperature distribution measured with the 84 thermistors and the ThermaWatch® Rotor is

Table 3

Heating pads power.

Heating pad	$q_{50 \text{ rpm}} (\text{W})$	$q_{300 \text{ rpm}} (\text{W})$
2	40.0	66.5
5	29.8	49.7
8	39.8	66.2
11	39.6	65.6
14	29.9	50.0
17	44.1	73.1
Total	223.2	371.0

specified as a boundary condition after performing a Kriging interpolation in order to assign a temperature value to each mesh node on the shell surface. Since temperatures on the outer pole surface may exceed 100 °C, radiation is taken into account in the numerical model by setting a negative source (heat sink) on the outer pole surface defined as follows:

$$q''_{\text{rad}} = \varepsilon \sigma (T_S^4 - T_\infty^4) \quad (1)$$

where ε is the surface emissivity (0.7) and σ is the Stefan–Boltzmann constant.

For both solvers, a second-order spatial discretization scheme and convergence criteria of 10^{-8} on the maximum residual value of the energy equation are specified. Since SYRTHES 4.0 is based on an unsteady algorithm, a constant time step of 1 s is used with a first-order time scheme. Convergence of the unsteady solver is used to reach the steady state.

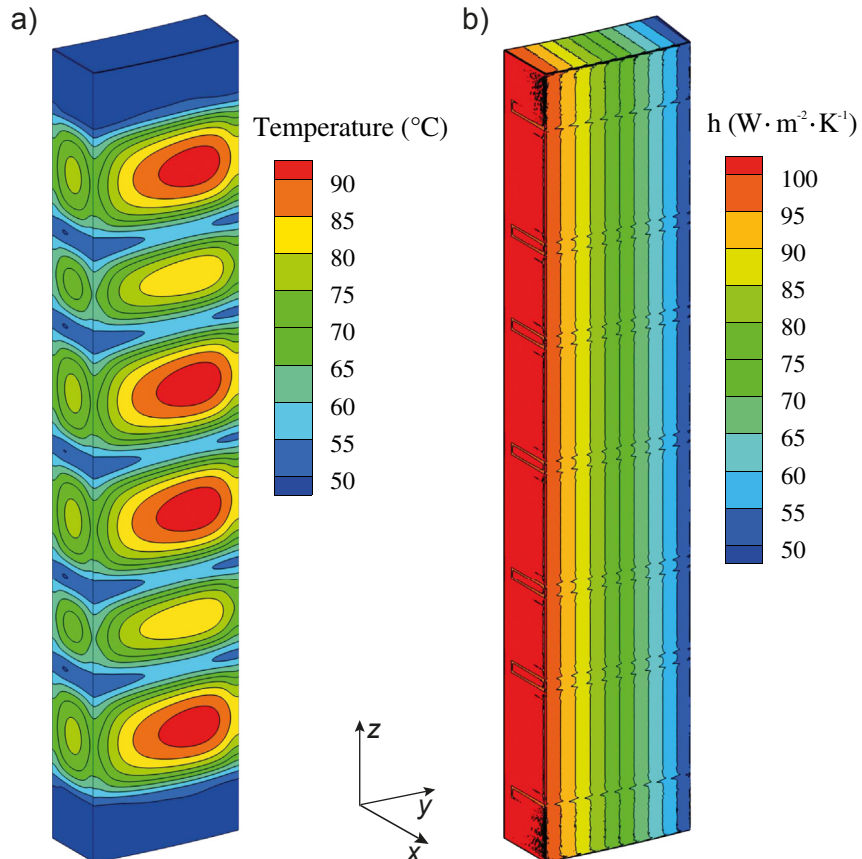


Fig. 7. Temperature (a) and heat transfer coefficient (b) distributions on the outer pole surface with Ansys-CFX.

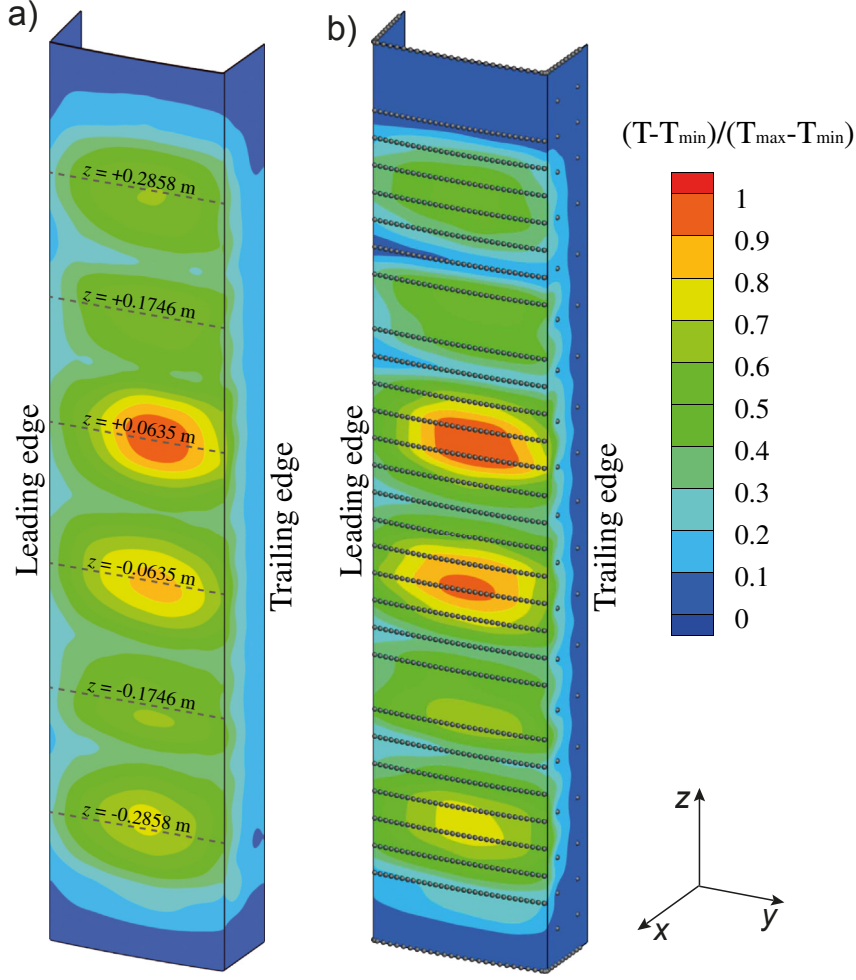


Fig. 8. Normalized temperature contours on the pole face at 50 rpm (a) and 300 rpm (b).

5. Numerical validation study

To validate the approach described above, a test case is run with the numerical domain shown in Fig. 6. A simulation is first performed with a specified linear heat transfer coefficient distribution on the outer pole surface ($h = 75\text{--}320.513 \text{ y}$) and an ambient air temperature of 44.8°C . An uniform heat source $q''' = 4.0 \times 10^6 \text{ W m}^{-3}$ is set for each heating element. On the inner surface of the supports, an equivalent heat transfer coefficient value is set in order to account for convection on this surface and for conduction since the inner section of each support is pressed between two steel rim plates (see Fig. 2a)).

As mentioned in Section 2, the pole shell is riveted to the aluminum supports and thus a thermal contact resistance ($R''_{t,c}$) between the two components must be considered, especially since both have a high thermal conductivity. A sensitivity study was performed to determine the impact of the thermal contact resistance on the pole heat flux distribution and the results are shown in Table 2. The reference value for an aluminum interface is $R''_{t,c} = 5.0 \times 10^{-4} \text{ m}^2 \text{ K W}^{-1}$ (from Ref. [9]).

The last column of Table 2 gives the heat flux value at the interface between the steel shell and the aluminum supports. As expected, for low $R''_{t,c}$ values, a relatively high fraction ($\sim 25\%$) of the heat flux generated by the pads is dissipated through the supports. However, when a high thermal contact resistance value is set at the interface, there is almost no heat flux toward the

supports. Although the $R''_{t,c}$ value has an impact on the heat flux distribution, in a range close to the reference value (i.e., $0.001 < R''_{t,c} < 0.0001$), the heat flux on the pole face and sides is only slightly affected (about 3% variation). This is reassuring since the exact $R''_{t,c}$ value for the scale model setup is not known due to many parameters (rivet pressure, surface roughness, centrifugal force, etc.) affecting the contact between the supports and the shell. Consequently, a $R''_{t,c} = 5.0 \times 10^{-4} \text{ m}^2 \text{ K W}^{-1}$ is used in all simulations.

After obtaining a converged solution from the first calculation, the computed temperature distribution on the outer pole surface (see Fig. 7(a)) is extracted and set as the boundary condition for a new simulation, while keeping all other parameters identical. The heat transfer coefficient distribution on the outer pole surface obtained by post-processing from the second simulation should then be equal to the initial linear distribution specified in the first computation.

As illustrated in Fig. 7(b), although there is a small amount of numerical noise near the shell supports, the heat transfer distribution obtained from the second simulation matches very closely the linear distribution initially set. The same results were obtained with SYRTHES 4.0 (not shown here) and the approach is thus validated for both solvers. The next step, discussed in the following section, is to use the measured temperature distribution on the pole surface as the boundary condition and to compute the inherent heat transfer coefficient distribution.

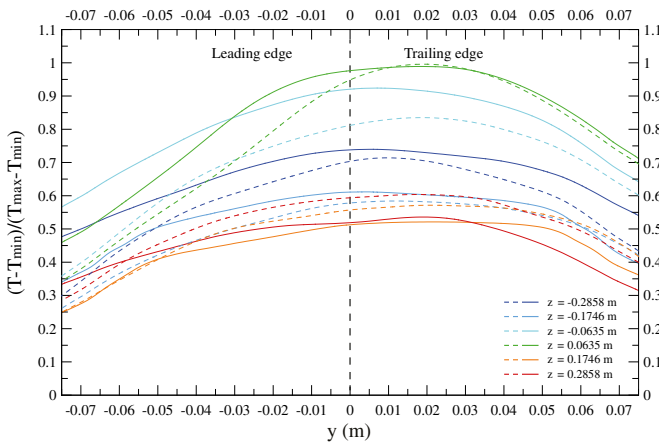


Fig. 9. Normalized temperature profiles on the pole face at 50 rpm (dashed lines) and 300 rpm (solid lines).

6. Results

Two experimental measurements are carried out at 50 and 300 rpm in order to determine the effect of rotation on the pole temperature distribution. The local Reynolds numbers based on the air gap dimension are 5000 and 30 000 at 50 and 300 rpm respectively. In both cases, only the six heating pads on the pole face were heated since measurements on the pole sides cannot be made with the ThermaWatch® Rotor probe, as explained in Section 3. Thermal stability was reached after 2 and 7 h for the 50 and 300 rpm cases respectively. The heat power generated by each pad is given in Table 3 and the power output was adjusted in order to obtain similar surface temperatures at both rotational speeds.

At steady state, the air temperature inside the scale model enclosure was 21.9 °C and 45.0 °C at 50 and 300 rpm respectively. This difference in ambient temperature is due to the windage losses, which are much higher at 300 rpm. The air temperature inside the pole shell itself was 40.1 °C and 56.8 °C at 50 and 300 rpm respectively. On the inner surface of the seven supports a uniform temperature of 24.6 °C and 48.7 °C at 50 and 300 rpm respectively was measured. This uniformity is due to the high thermal mass of the rim. Lastly, on the bottom pole cover a temperature of 24.6 °C

and 49.1 °C at 50 and 300 rpm was measured and on the top cover the temperatures were 24.9 °C and 48.9 °C respectively.

Figs. 8 and 9 show the normalized temperature contours and profiles measured on the pole surface at 50 and 300 rpm. The dashed lines in Fig. 8(a) show the position along which the profiles were plotted whereas the grey dots in Fig. 8(b), show the points used by the Kriging algorithm to interpolate the measured values over the entire pole surface. At both rotational speeds, the location of the maximum temperature shifts toward the trailing edge of the pole surface. This asymmetry is due to the flow dynamics since a recirculation zone is probably present near the trailing edge of the pole. In this region of low air velocity, cooling is thus less efficient and it causes a local increase in temperature. Moreover, the pole sides are always at lower temperatures than the central region since additional cooling is provided by the flow exiting the rim ducts. Though these phenomena have been previously observed on actual generators and reported in the literature, the number of sensors in past studies was not sufficient to obtain a complete temperature mapping of the pole.

In the axial direction, a strong gradient is present with temperatures at the center of the pole face about 25 °C higher than at the ends even though the injected heat fluxes are almost identical. This is due to the top and bottom fans which generate an axial flow in the air gap and interpolate resulting in an additional cooling in this region. Moreover, the flow generated by the fans tends to uniformize the temperature profile across the pole face and to mask rotational effects between the leading and trailing edges.

Another axial asymmetry feature is present since the temperature profiles near the bottom end of the pole (i.e., $z = -0.2858$ m and $z = -0.1746$ m) show higher values compared to corresponding positions at the top end. This difference is partly due to slightly higher heat power in pad 17 but also to geometrical asymmetry in the rotor spider and the rotor air inlets. As shown in Fig. 1, the rotor spider arm does not cover the entire pole height and in the lower portion it only consists of a triangular plate. Furthermore, due to the configuration of the rotor top and bottom inlets, a larger fraction of the total air mass flow rate tends to pass through the former opening.

Using the approach described in the previous section, the heat transfer coefficient distribution has been computed and the profiles at six axial positions are presented in Fig. 10 and Fig. 11 for the 50 and 300 rpm cases respectively. Firstly, it is observed that the h values at 50 rpm are about four times smaller than at 300 rpm since, as expected, flow velocities near the pole surface are lower at 50 rpm. Moreover, it is interesting to notice that at 50 rpm the heat

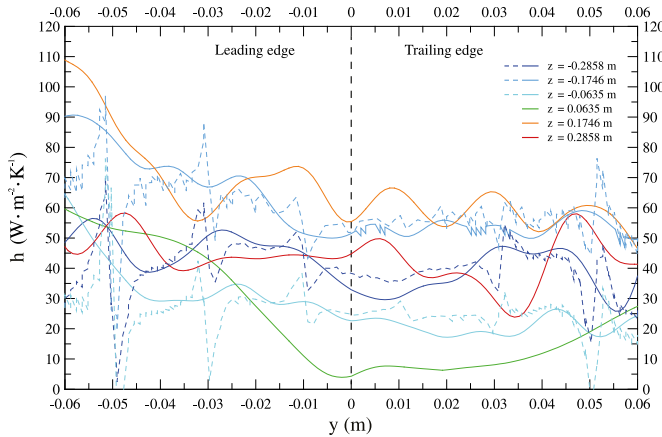


Fig. 10. Heat transfer coefficient profiles on the pole face at 50 rpm (Ansys-CFX: solid lines; SYRTHES 4.0: dashed lines).

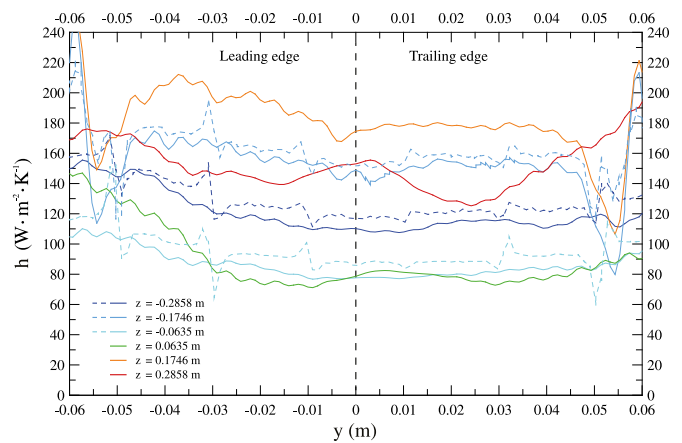


Fig. 11. Heat transfer coefficient profiles on the pole face at 300 rpm (Ansys-CFX: solid lines; SYRTHES 4.0: dashed lines).

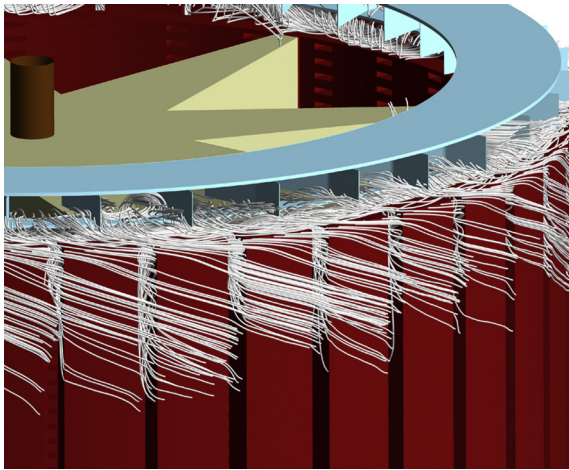


Fig. 12. Streamlines near the pole top end at 300 rpm (from Ansys-CFX).

transfer coefficient at $z = \pm 0.1746$ m is about 50% higher than at $z = \pm 0.2858$ m and at 300 rpm this difference is about 25%. This may seem surprising since the profiles at $z = \pm 0.2858$ m are closer to the fans. However, the streamlines in Fig. 12 obtained from a preliminary CFD study of ventilation in the scale model (not presented here since beyond the scope of this paper) show that the flow generated by the top radial fans mainly enters the interpole space and only after penetrating a certain distance in the axial direction it exits through the air gap and goes around the pole face. The same phenomenon occurs at the lower end of the rotor and thus the intermediate pole face sections (i.e., at $z = \pm 0.1746$ m) are better cooled than the top end sections (i.e., at $z = \pm 0.2858$ m).

Lastly, the plots show that the heat transfer coefficient profiles computed with Ansys-CFX and SYRTHES 4.0 are quite similar, though the noise level appears to be greater with the latter code (for clarity purposes only the bottom three positions are shown for SYRTHES 4.0). A possible explanation is that a hexahedral mesh was used for Ansys-CFX while a tetrahedral grid was required by SYRTHES 4.0 for which the element skewness may induce a certain level of noise in the numerical solution, particularly in derived quantities such as the heat transfer coefficient.

In summary, using the approach presented in this paper, the heat transfer coefficient distribution on a rotor pole face was obtained and it was observed that rotation has a noticeable impact on heat transfer mechanisms. The next step will be to perform a 3D CHT simulation of the IREQ scale model and to compare computed h values with those obtained in this study. This will validate the numerical tools with the intent to subsequently use them to obtain a global mapping of the heat transfer coefficient on hydrogenerator prototypes. Moreover, by coupling the thermofluid model with an electromagnetic model providing heat losses, it will be possible to evaluate pole temperatures and ultimately deduce generators operational limits when the hot-spot is on the rotor.

7. Conclusion

This study showed how a hybrid numerical-experimental approach can be used to investigate the effect of rotation on the cooling of a hydrogenerator scale model pole. The measurements have shown that the temperature profile on the pole face is asymmetric in the tangential direction with maximum temperatures closer to the trailing edge. This local overheating is due to a recirculation zone where slow moving fluid cools the pole surface less efficiently. Moreover, a strong temperature gradient is

observed in the axial direction due to the presence of fans that improve cooling at the top and bottom ends of the pole. By post-processing the numerical results from Ansys-CFX and SYRTHES 4.0, the heat transfer coefficient profile along the pole face has been obtained at six different axial positions along the pole. Results show that h values are about four times higher at 300 rpm than at 50 rpm. Furthermore, the heat transfer coefficients at the uppermost and lowermost axial locations on the pole face (i.e., closest to the top and bottom fans) have a lower value than at the corresponding adjacent locations since the flow generated by the fans enters the interpole space and only after penetrating a certain distance in the axial direction it exits through the air gap and goes around the pole face.

In the future, a 3D conjugate heat transfer simulation of the scale model will be performed and the numerical values for the heat transfer coefficient on the pole surface will be compared to the experimental data obtained in this study. This will validate of the numerical tools that will ultimately be used to perform thermofluid analysis of hydrogenerator prototypes.

References

- [1] A. Boglietti, A. Cavagnino, D. Staton, M. Shanel, M. Mueller, C. Mejuto, Evolution and modern approaches for thermal analysis of electrical machines, *IEEE Trans. Ind. Electron.* 56 (2009).
- [2] N.J. Carew, Experimental determination of heat transfer coefficients of salient pole rotors, *Therm. Aspects Mach.* IEEE (1992) 1–8.
- [3] G. Djaku, D. Gerling, An improved lumped parameter thermal model for electrical machines, in: Proceedings of the 17th International Conference on Electrical Machines, Chania, Greece, 2006.
- [4] R. Díez, R. Zickermann, A. Schwery, A. Avellan, CFD validation and air cooling design methodology for large hydro generator, in: Proceedings of the 17th International Conference on Electrical Machines, Chania, Greece, 2006.
- [5] Z.N. Fan, L. Han, G.H. Zhou, X.Q. Hou, Y.G. Liao, Loss and heat computations of damper bars in large tubular hydro-generator, in: Proceedings of the 11th International Conference on Electrical Machines and Systems, Wuhan, China, 2008.
- [6] A. Fasquelle, J. Le Besnerais, S. Harmand, M. Hecquet, S. Brisset, P. Brochet, A. Randria, Coupled electromagnetic acoustic and thermal flow modeling of an induction motor of railway traction, *Appl. Therm. Eng.* 30 (2010) 2788–2795.
- [7] M. Fénot, E. Dorigac, A. Giret, G. Lalizel, Convective heat transfer in the entry region of an annular channel with slotted rotating inner cylinder, *Appl. Therm. Eng.* 54 (2013) 345–358.
- [8] C.-H. Huang, H.-C. Lo, A three-dimensional inverse problem in estimating the internal heat flux of housing for high speed motors, *Appl. Therm. Eng.* 26 (2006) 1515–1529.
- [9] F.P. Incropera, D.P. DeWitt, *Fundamentals of Heat and Mass Transfer*, John Wiley and Sons, 2002.
- [10] G. Kastner, E. Farnleitner, M. Brunner, Usage of computational fluid dynamics in the ventilation design process for prototype hydro-generators, in: Proceedings of the 16th International Seminar on Hydropower Plants, Vienna, Austria, 2010.
- [11] H. Lang, C. Kral, A. Haumer, M. Haigis, R. Schulz, Investigation of the thermal behavior of a salient pole synchronous machine, in: Proceedings of the 17th International Conference on Electrical Machines, Chania, Greece, 2006.
- [12] K. Murata, S. Nonaka, M. Yamamoto, Y. Takeda, Experimental study on cooling of rotor in a salient 4-pole synchronous machine, *IEEE Trans. Power Apparatus Syst.* 98 (1979) 310–317.
- [13] S.J. Pickering, D. Lampard, M. Shanel, Modelling ventilation and cooling of the rotors of salient pole machines, in: IEEE International Conference on Electric Machines and Drives, 2001, pp. 806–808.
- [14] W. Robinson, F.S. Tse, Surface heat-transfer coefficients of salient poles in a blast-cooled alternator, *Trans. Am. Inst. Electr. Eng.* 76 (1957) 199–204.
- [15] I. Rupp, C. Peniguel, SYRTHES 4.0-User Manual, EDF, 2012.
- [16] M. Shanel, S.J. Pickering, D. Lampard, Conjugate heat transfer analysis of a salient pole rotor in an air cooled synchronous generator, in: IEEE International Conference on Electric Machines and Drives, 2003, pp. 737–741.
- [17] G. Traxler-Samek, R. Zickermann, A. Schwery, Cooling airflow, losses, and temperatures in large air-cooled synchronous machines, *IEEE Trans. Ind. Electron.* 57 (2010) 172–180.
- [18] R. Ujije, R. Arlett, H. Etoh, Application of computational fluid dynamics (CFD) on ventilation-cooling optimization of electrical machines, *Rev. Energy Technol. Generation Transm. Distribution Electr. Therm. Energy* (2006) 17–22.
- [19] B. Vogt, S. Lahres, Calculation of cooling and ventilation of large hydro generators with advanced 3d numerical methods, in: Proceedings of the International HYDRO Conference, Innsbruck, Austria, 2013.
- [20] L. Weili, G. Chunwei, Z. Ping, Calculation of a complex 3-D model of a turbogenerator with end region regarding electrical losses, cooling, and heating, *IEEE Trans. Energy Convers.* 26 (2011) 1073–1080.